

1 **Is oceanic buffering of forced ITCZ shifts controlled by an**
2 **underappreciated Atlantic meridional overturning circulation pathway?***

3 Sungduk Yu* and Michael S. Pritchard

4 *Department of Earth System Sciences, University of California, Irvine, California, 92697.*

5 *Corresponding author address: Department of Earth System Sciences, University of California,
6 Irvine, California, 92697.

7 E-mail: sungduk@uci.edu

*This work has been submitted for publication. Copyright in this work may be transferred without further notice, and this version may no longer be accessible.

ABSTRACT

8 Ocean circulation responses to interhemispheric radiative imbalance can
9 damp north-south migrations of the intertropical convergence zone (ITCZ),
10 by reducing the burden on atmospheric heat transport. The role of the At-
11 lantic meridional overturning circulation (AMOC) in such dynamics has not
12 received much attention. Here, we show coupled climate modeling results that
13 suggest AMOC responses are of first order importance to muting ITCZ shift
14 magnitudes as a pair of solar forcing bands is moved from equatorial to polar
15 latitudes. The cross-equatorial energy transport response to the same amount
16 of interhemispheric forcing becomes systematically more ocean-centric when
17 higher latitudes are perturbed in association with strengthening AMOC re-
18 sponses. In contrast, the responses of the Pacific Subtropical Cell are not
19 monotonic and cannot predict this variance in the ITCZ's equilibrium posi-
20 tion. Overall these results highlight the importance of the meridional distri-
21 bution of interhemispheric radiative imbalance and the rich buffering of in-
22 ternal feedbacks that occurs in dynamical versus thermodynamic slab ocean
23 modeling experiments. Mostly, the result implies that the problem of devel-
24 oping a theory of ITCZ migration is entangled with that of understanding the
25 AMOC's response to hemispherically asymmetric radiative forcing—a diffi-
26 cult topic deserving of focused analysis across more climate models.

27 **1. Introduction**

28 The intertropical convergence zone (ITCZ) is a band of intense rainfall encircling most of the
29 tropics, roughly coinciding with the ascending branch of the Hadley Cell. Even a minor shift of its
30 location (or change of its intensity) matters to society as this can result in major fluctuations of re-
31 gional water availability in the tropics as well as impacting the extratropics through changes in the
32 frequency of tropical cyclones (Dunstone et al. 2013; Merlis et al. 2013) and shifts of the midlati-
33 tude jet (Ceppi et al. 2013; Cvijanovic et al. 2013). The zonal-mean position of the ITCZ is largely
34 constrained by interhemispheric energy imbalance of the atmosphere because the thermally-direct
35 Hadley cell transports heat following the direction of its upper branch (i.e. the energetics frame-
36 work; see Schneider et al. (2014) and Kang et al. (2018) for reviews). That is, the ITCZ resides in
37 the warmer hemisphere so that its upper branch crosses the equator, helping transport heat to the
38 colder hemisphere. Transient ITCZ migrations toward an anomalously warmed hemisphere can
39 occur in response to external forcing over a multitude of timescales, from seasonal to millennial
40 (Donohoe et al. 2013; Schneider et al. 2014).

41 It is imperative to better understand such ITCZ shift dynamics, and especially the role of the
42 ocean, which has been receiving increased attention. Recent global climate model (GCM) experi-
43 ments have shown that oceanic dynamics can damp ITCZ shift responses to high-latitude forcing
44 by imposed cloud brightness (Kay et al. 2016), ocean albedo (Hawcroft et al. 2016), sea-ice cover
45 (Tomas et al. 2016), and stratospheric aerosols (Hawcroft et al. 2018). This is in contrast to studies
46 that do not include ocean dynamics (e.g. Chiang and Bitz 2005; Broccoli et al. 2006; Kang et al.
47 2008) which exhibit more pronounced ITCZ shifts to extratropical forcings. This occurs since
48 perturbations to interhemispheric energy balance need not be restored by the atmosphere alone in
49 a dynamic ocean coupled GCM; they can also be mediated by changes in oceanic heat transport.

50 The mechanical coupling between the Hadley cell and the oceanic subtropical cell (STC) via zonal
51 surface wind stress has been attributed to one such damping effect (Held 2001; Schneider et al.
52 2014; Green and Marshall 2017; Schneider 2017; Kang et al. 2018). But the role of STC damping
53 relative to other potentially important oceanic damping pathways, such as the Atlantic meridional
54 overturning circulation (AMOC), remains unclear. Yet theoretical arguments that the AMOC is
55 fundamental to controlling the annual mean ITCZ location (Frierson et al. 2013; Marshall et al.
56 2014) motivate its potential importance.

57 Several modeling studies already suggest important links between the AMOC and the ITCZ
58 position. It has been known for decades that coupled GCM experiments subjected to freshwater
59 hosing in the North Atlantic exhibit southward shifts of the ITCZ in association with a weakened
60 AMOC (Manabe and Stouffer 1995; Vellinga and Wood 2002; Zhang and Delworth 2005; Chang
61 et al. 2008; Zhang et al. 2010; Drijfhout 2010). More recently, Fukar et al. (2013) argued that
62 AMOC-type circulations determine the zonal-mean ITCZ position in an idealized limited-domain
63 coupled GCM. Building on this work, Frierson et al. (2013) and Marshall et al. (2014) showed
64 the ITCZ position's annual mean tendency to lie north of the equator is a result of AMOC heat
65 transport, using a combination of slab ocean aquaplanet and idealized global coupled GCM, along
66 with observational analysis. Other studies allude to an important role of the AMOC in the ITCZ
67 shift response to aerosol clean-up projected over the 21st century. For instance, the projected
68 northward ITCZ shift due to relative warming of the North Atlantic from regional aerosol clean-
69 up is shown to be smaller in the Atlantic than in the Pacific (Rotstayn et al. 2015; Allen 2015) and
70 counteracted by weakening of AMOC (i.e. cooling of the North Atlantic), ultimately muting the
71 shift of annual-mean ITCZ position (AA and Frierson 2017).

72 The above studies all hint at the potential for ITCZ shifts to be modulated by the AMOC's
73 response to external radiative forcing. But questions remain about how significant this AMOC-

74 linked pathway is. Indeed, much is yet to be discovered about how the AMOC responds in general
75 to geographically structured radiative forcing at top of atmosphere, as can occur through latitudi-
76 nally sensitive cloud feedbacks to climate change, or some volcanoes, or through geoengineering
77 by solar radiation management. Yet this may have implications for ITCZ shift dynamics.

78 We hypothesize that the AMOC can play an important role for muting ITCZ shift in this con-
79 text. Conceptually this is based on the fact that on long (greater than interannual) timescales the
80 AMOC variability is driven by thermodynamic forcing (Buckley and Marshall 2016). This is in
81 contrast to wind-driven variations in other circulation components such as the STC, whose vari-
82 ability is mainly driven by mechanical forcing via surface wind stress (JP and Lu 1994; Liu and
83 Philander 1995). A consequence of mechanical coupling in the STC is that the cross-equatorial
84 atmospheric and oceanic energy transports must positively covary (as illustrated in Fig. 1a and b).
85 That is, the partitioning between atmospheric and oceanic responses cannot vary much through
86 the STC coupling, assuming oceanic thermal structures do not change much. The AMOC is not
87 subject to this mechanical constraint; rather its heat transport has the capacity to covary negatively
88 with a given top-of-atmosphere heating imbalance (as illustrated in Fig. 1c and d). Thus, if the
89 AMOC responded sensitively to the details of how a hemispherically asymmetric external forcing
90 were geographically distributed, this could potentially act as an efficient control on ITCZ shift
91 damping efficiency, associated with changes in the overall ocean-atmosphere partitioning of the
92 cross-equatorial energy transport response.

93 To probe this issue, we present results from a coupled climate model experiment, in which we
94 artificially alter the top-of-atmosphere (TOA) energy budget through solar radiation modulation
95 focused in discrete latitudinal bands at varying distances from the equator (Fig. 2a). The TOA
96 insolation is perturbed to induce a northward heat transport by increasing (decreasing) the solar
97 constant in the southern (northern) hemisphere. Such a perturbation is introduced at four dif-

98 ferent latitudinal bands (TROP, SUBTROP, MIDLAT, and HIGHLAT) occupying an equal area
99 to examine partitioning responses to the different forcing locations. One additional experiment
100 perturbing the whole hemisphere at a quarter of the magnitude (i.e. identical interhemispheric
101 power asymmetry) is also performed (WHOLE). TOA forcing allows freedom for the simulated
102 climate system to internally select its preferred partitioning of heat transport responses between
103 the atmosphere and ocean (and, within the ocean, between AMOC vs. other ocean circulation
104 components). Our forcing is in some ways similar to Mechoso et al. (2016) (solar flux alteration)
105 and Haywood et al. (2016); Hawcroft et al. (2018) (stratospheric aerosol management), but also
106 with three notable differences—(i) we only perturb non-UV part of solar radiation to avoid a di-
107 rect stratospheric perturbation, (ii) we avoid net global perturbation by introducing both solar flux
108 source and sink, and (iii) we integrate for long enough to sample AMOC responses (200 years,
109 compared to 20 (Haywood et al. 2016), 25 (Mechoso et al. 2016), and 80 (Hawcroft et al. 2018)
110 years).

111 Consistent with our hypothesis, the results will reveal a strong correlation between the mag-
112 nitude of AMOC responses and the meridional distribution of interhemispheric forcing, which
113 in turn explains a large degree of variance in the degree of ITCZ shift response that occurs at
114 equilibrium.

115 **2. Method**

116 *a. GCM simulations*

117 The Community Earth System Model (CESM) version 1.2.2. (Hurrell et al. 2013) is used,
118 configured with interactive atmosphere, land, ocean and sea ice components in a preindustrial ex-
119 periment mode initialized with a spun-up ocean (i.e. the standard “B_1850_CAM5” component

120 set). A set of five experiments that induce interhemispheric energy imbalance at top of the sim-
 121 ulated atmosphere (TOA), but in different latitude ranges, by dividing each hemisphere into four
 122 zonal bands of equal area, eg. tropical, subtropical, mid-latitude, and high-latitude zones. The
 123 four experiments are called TROP, SUBTROP, MIDLAT and HIGHLAT hereafter. In addition,
 124 we perform an extra experiment (WHOLE) of which the whole hemisphere is perturbed but at
 125 a quarter magnitude in order to keep the area-integrated perturbation identical to other cases. A
 126 control simulation (CTRL) is conducted with no perturbation for the same period as experimental
 127 simulations. In each test, we introduce an artificial incoming non-UV shortwave energy source
 128 / sink pair at the TOA in the southern / northern hemisphere, of magnitude 17 W m^{-2} in annual
 129 mean—by multiplying a constant factor, not adding, in order to prevent exceedingly high pertur-
 130 bation during winter. Our decision to position our forcing at TOA is attractive philosophically
 131 as it maximizes the simulated climate system’s freedom to excite internal feedbacks and to inter-
 132 nally select the partitioning of the meridional energy transport response between atmosphere and
 133 ocean. Each simulation is integrated for 200 years, but the last 150 years of simulations are used
 134 for the analysis in this paper, unless otherwise noted. Model simulation output and model code
 135 modification are available upon request.

136 *b. Meridional energy transport calculation*

137 The total (atmospheric plus oceanic) meridional heat transport, F , is calculated as

$$F(\phi) = - \int_{\phi}^{\pi/2} \int_0^{2\pi} \left[R_{TOA} - \frac{\partial(E_A)}{\partial t} - \frac{\partial(E_O)}{\partial t} \right] a^2 \cos\phi d\theta d\phi,$$

138 where R_{TOA} is a residual radiative flux at TOA, E_A (E_O) is a column energy storage of atmosphere
 139 (ocean), a is the Earth radius, and θ and ϕ are longitude and latitude, respectively. Zonally-
 140 integrated meridional oceanic heat transport, F_O , is directly calculated from the ocean model by

141 summing advective and diffusive fluxes over depth and longitude at each latitude. Meridional
142 atmospheric heat transport, F_A , is calculated as a residual, e.g. $F_A = F - F_O$.

143 *c. Oceanic heat transport decomposition*

144 Cross-equatorial OHT is decomposed into into its dynamic ($T_{ctrl}\Delta v$), thermodynamic ($v_{ctrl}\Delta T$),
145 and nonlinear components ($\Delta v\Delta T$),

$$\Delta(vT) = T_{ctrl}\Delta v + v_{ctrl}\Delta T + \Delta v\Delta T,$$

146 where v is meridional velocity, T is temperature, $\Delta(\dots) = (\dots)_{exp} - (\dots)_{ctrl}$, and subscript exp
147 (ctrl) means experiment (control) simulation result.

148 *d. Tropical precipitation asymmetry index (PAI)*

149 Following Hwang and Frierson (2013), precipitation asymmetry index is calculated as the area-
150 weighted mean precipitation rate difference between north (0° to 20°N) and south (20°S to 0°),
151 then normalized by the area-weighted mean precipitation rate of the whole tropics (20°S to 20°N).
152 Accordingly, the PAI captures the relative strength of the two solstice season ITCZ positions, as
153 which we define the position of *annual-mean* ITCZ. The responses of PAI are well-correlated
154 with that of the tropical precipitation centroid (Fig. S1), which is another popular measure of
155 annual-mean ITCZ position.

156 **3. Results**

157 We begin by analyzing the annual-mean ITCZ precipitation response across the experiment en-
158 semble using the last 150-year average. A southward ITCZ “shift”, a term we will use as shorthand
159 to describe an increase (decrease) in intensity of the southern (northern) zonal-mean, annual-mean
160 rainfall band, is observed in all cases, as expected by the northward cross-equatorial atmospheric

161 heat transport (AHT) response to warming (cooling) the southern (northern) hemisphere. How-
162 ever, its magnitude monotonically decreases as the forcing bands are moved poleward (Fig. 2b).
163 This differing ITCZ shift response occurs *despite* the fact that the magnitude of incoming solar
164 forcing asymmetry is constrained to be identical across the experiments. This implies that either
165 (i) latitudinally varying internal radiative feedbacks modify the effective magnitude of the asym-
166 metric forcing across experiments; and/or (ii) the cross-equatorial oceanic heat transport (OHT)
167 response is sensitive to the geographic details of the forcing. While the effective forcing (i.e.
168 including radiative feedbacks), which mostly determines the cross-equatorial total heat transport
169 since oceanic heat content change is very small (Fig. 3), does show some variation across exper-
170 iments, there is remarkably little spread in its net interhemispheric asymmetry (Fig. 2b) with a
171 range of 2.90–3.38 W m⁻² as a result of compensating internal radiative feedbacks (Fig. 3). This
172 is interestingly inconsistent with the results of Seo et al. (2014), in which latitudinally sensitive
173 cloud feedbacks are able to exert strong control of AHT due to the use of a slab ocean model;
174 the implication is that dynamic oceanic buffering is important to this issue. For our own purposes
175 the main point is that such internal radiative feedback can only explain about 0.12 PW spread
176 in the total (oceanic plus atmospheric) cross-equatorial heat transport response, arguing against
177 (i). In contrast the spread of AHT alone is much larger (Fig. 2c), implying that variability in
178 the annual-mean ITCZ shift response is mainly driven by variability in OHT responses across the
179 experiments.

180 So far we have found that the cross-equatorial heat transport partitioning between ocean and
181 atmosphere becomes a key factor that determines the magnitude of ITCZ shift in our experiments:
182 When interhemispherically asymmetric solar forcing is concentrated at higher latitudes, the par-
183 titioning of the coupled response becomes more ocean-centric and thus the ITCZ shift response
184 becomes more muted. The question naturally arises as to why.

185 Before proceeding, we first confirm that it is appropriate to view relationships between AHT and
186 ITCZ across our experiments through an energetics framework. This acknowledges that there can
187 be special cases where such a framework can be inappropriate, for instance if the heat transport
188 efficiency of the Hadley circulation (i.e. the gross moist stibility, GMS) dominates spread in the
189 AHT response (Seo et al. 2017) or if the eddy heat transport dominates spread in the time mean
190 Hadley circulation heat transport (Roberts et al. 2016). However, in our case, the cross-equatorial
191 AHT response is a good proxy for a zonal-mean ITCZ shift response. A tight linear relationship
192 between the cross-equatorial AHT and the mean meridional circulation (Hadley circulation) re-
193 sponses show GMS responses are secondary (Fig. 4), and the eddy heat transport (transient plus
194 stationary) responses are much weaker than Hadley cell heat transport and scale with the strength
195 of Hadley circulation (Fig. 5). Thus a time-mean energetics framework is appropriate to apply in
196 our analysis.

197 Fig. 6 shows that Atlantic dynamics play a leading role in driving the tendency towards a more
198 ocean-centric energy transport response with higher latitude forcing. To understand the role of
199 each ocean, the basin-specific OHT responses are decomposed into dynamic and thermodynamic
200 components (Fig. 6). The OHT responses to changing the latitudinal position of hemispherically
201 asymmetric forcing are mostly driven by dynamic changes, not thermodynamic. But different
202 ocean basins respond differently. Only the Atlantic shows a clear monotonic sensitivity across
203 experiments in line with the global OHT sensitivity. In contrast, the Pacific-Indian OHT does
204 not exhibit a monotonic sensitivity, except during the transition from SUBTROP to MIDLAT,
205 during which both Atlantic and Pacific-Indian basins show comparable OHT increases. Despite
206 the fact that the absolute magnitude of the Atlantic OHT response is generally smaller than that of
207 the Pacific-Indian, normalized by its respective basin width the Atlantic is a much more efficient
208 energy transporter (yellow dots in Fig. 6) and seems to play a controlling role in the experiments.

209 This draws our analysis toward the Atlantic meridional overturning circulation (AMOC), as the
210 main dynamical pathway of meridional oceanic heat transport in the Atlantic. Consistent with the
211 Atlantic OHT, the AMOC response becomes monotonically stronger as the solar forcing bands are
212 moved poleward (Fig. 7a). Transient analysis shows this monotonic sorting with forcing latitude
213 emerges within 30 years (Fig. 8a) and persists for two centuries amidst internal variability. There
214 is reassuring consistency in the unsteady evolution of the anomalous Atlantic OHT and AMOC
215 strength (Fig. 8a and b).

216 Unlike the AMOC responses, the Pacific-Indian STC responses do not exhibit a monotonic sen-
217 sitivity with implications for total cross-equatorial OHT (Fig. 8c). While tantalizing changes in
218 the STC circulation response do occur (Fig. 7b, and hemispherically asymmetric component in
219 Fig. S2), no associated cross-equatorial OHT responses are detectable (Fig. 8d). This implies
220 internal compensations in the structure of the shallow overturning circulation’s response buffer its
221 overall interhemispheric energetics. The buffering mechanisms are case specific. For instance, in
222 HIGHLAT, despite the fact that a weakening of the STC mass circulation response might act to
223 reduce its OHT relative to CTRL, this is compensated by a deepening of the circulation indicating
224 increasing vertical thermal contrast—in turn implying more efficient heat transport per unit over-
225 turning circulation, thus acting to increase OHT in resistance to the weaker circulation. A separate
226 mechanism buffers the TROP experiment, via spinup of a strong cross-equatorial roll-type circu-
227 lation near the equator (Miyama et al. 2003) that acts against weakened STC mass circulation, in
228 this case through a mechanism that is independent of the STC’s depth.

229 *Different timescale between Pacific and Atlantic Mechanism*

230 In Fig. 9, scatter plots of key predictors of tropical precipitation asymmetry both within ex-
231 periments (i.e. dots of one color) and across experiments (i.e. dots spanning multiple colors)

232 provide an especially compact way to contrast the differing roles of the two ocean basins on mul-
233 tidecadal (top) vs. interannual (bottom) timescales. On long timescales, the decomposition of
234 the global relationship between PAI and OHT shows that the Atlantic clearly controls the equi-
235 librium state response to the TOA forcing (monotonic color ranking along statistically significant
236 inter-experiment regression line in Fig. 9a, b), whereas the Pacific-Indian OHT cannot detectably
237 predict global PAI variance within noise (Fig. 9c). However, on short timescales, a robust re-
238 gression is detected within each experiment between Pacific-Indian OHT and global PAI (colored
239 regression lines in Fig. 9d, f). This timescale separation between the two ocean basins is robust to
240 variations of the exact running mean windows used to discriminate short- from long-term behav-
241 ior, although the long-term Atlantic correlation reaches its maximum around a 10-year averaging
242 window (Fig. 9g).

243 The opposite signs of the PAI–OHT correlation for the Atlantic (across experiments) versus
244 the Pacific-Indian (within experiments) illustrate the fundamental difference of AMOC vs. STC
245 freedom to damp ITCZ shifts that was alluded to in the introduction and Fig. 1. Keeping in mind
246 that a more negative PAI implies a more southward ITCZ position and a more positive (northward)
247 cross-equatorial AHT (Fig. 10), the regressions in Fig. 9 show that Atlantic OHT negatively
248 covaries with AHT, whereas Pacific-Indian OHT positively covaries with AHT. This confirms
249 our hypothesis that an AMOC response has the capacity to be an efficient ITCZ shift damping
250 mechanism, as it can significantly alter the partitioning between atmospheric and oceanic heat
251 transport.

252 We note that the cross-experiment correlation between the PAI and the Atlantic OHT_{eq} responses
253 (Fig. 9b) does not depend on the fact that the magnitude of effective forcing (forcing + radiative
254 feedbacks)—which dictates the total heat transport (TotalHT) magnitude—happens to have been
255 similar across our experiments (e.g. Fig. 2c). While the response magnitudes of ΔAHT_{eq} and

256 $\Delta\text{OHT}_{\text{eq}}$ are constrained by the effective forcing magnitude ($\Delta\text{AHT}_{\text{eq}} + \Delta\text{OHT}_{\text{eq}} = \Delta\text{TotalHT}_{\text{eq}}$),
 257 the *partitioning* between $\Delta\text{AHT}_{\text{eq}}$ and $\Delta\text{OHT}_{\text{eq}}$ is not, i.e.

$$\frac{\Delta\text{AHT}_{\text{eq}}}{\Delta\text{TotalHT}_{\text{eq}}} + \frac{\Delta\text{OHT}_{\text{eq}}}{\Delta\text{TotalHT}_{\text{eq}}} = 1, \quad (1)$$

258 implying that the negative covariance between the normalized quantities is guaranteed despite the
 259 fact that the covariance of the un-normalized quantities depends on the magnitude of $\Delta\text{TotalHT}_{\text{eq}}$.

260 Assuming that the Hadley Circulation heat transport dominates the cross-equatorial atmospheric
 261 heat transport ($\Delta\text{AHT}_{\text{eq}} = \Delta\text{AHT}_{\text{eq}}^{\text{HC}} + \Delta\text{AHT}_{\text{eq}}^{\text{EDDY}} \approx \Delta\text{AHT}_{\text{eq}}^{\text{HC}}$; Fig. 5), that the cross-equatorial
 262 oceanic heat transport is mostly driven by two overturning circulations ($\Delta\text{OHT}_{\text{eq}} \approx \Delta\text{OHT}_{\text{eq}}^{\text{STC}} +$
 263 $\Delta\text{OHT}_{\text{eq}}^{\text{AMOC}}$), and that $\text{AHT}_{\text{eq}}^{\text{HC}}$ and $\text{OHT}_{\text{eq}}^{\text{STC}}$ are coupled ($\Delta\text{OHT}_{\text{eq}}^{\text{STC}} \approx \alpha\Delta\text{AHT}_{\text{eq}}^{\text{HC}}$; Held (2001)),

264 Eq. 1 can be simplified to

$$(1 + \alpha) \frac{\Delta\text{AHT}_{\text{eq}}^{\text{HC}}}{\Delta\text{TotalHT}_{\text{eq}}} + \frac{\Delta\text{OHT}_{\text{eq}}^{\text{AMOC}}}{\Delta\text{TotalHT}_{\text{eq}}} = 1, \quad (2)$$

265 where the superscripts HC, EDDY, STC, and AMOC denote heat transport components due to the
 266 Hadley Circulation, eddies, the subtropical cell, and the Atlantic meridional circulation, respec-
 267 tively, and α is a positive definite function. Accordingly, we expect to see a similarly tight, if not
 268 tighter, correlation when normalizing OHT_{eq} by the effective forcing magnitude; indeed this is
 269 confirmed in Fig. S3.

270 4. Discussion

271 The many internal feedbacks in our experiments have led to behaviors worth contrasting against
 272 the intuition gained from slab ocean modeling setups, which would not have predicted them. For
 273 instance, using a slab-ocean coupled GCM forced by a prescribed oceanic heat transport, Seo et al.
 274 (2014) showed amplifying TOA energy imbalance and hence a larger ITCZ shift with higher lati-
 275 tude perturbation, and explained this as a result of net positive SST–low cloud, SST–outgoing long-

276 wave radiation (OLR) feedbacks. Despite the fact that similar SST-mediated radiative feedbacks
277 also exist in our study, we observe a TOA energy imbalance that is largely insensitive to forcing
278 latitude. This can be traced to the fact that we observe a much weaker SST response magnitude
279 (Fig. 11a) in our more heavily buffered system. For instance, our SST response for HIGHLAT is
280 about 3 K, but this is an order of magnitude smaller than Seo et al. (20–80 K) despite the fact that
281 their forcing magnitude is only 1.64 times larger than in our experiment. A decomposition of the
282 details shows that for our high latitude forcing cases (MIDLAT and HIGHLAT), the SST–OLR
283 negative feedback actually wins over the positive SST–low cloud feedback. This underscores that
284 important positive feedbacks that were not included in the setup of Seo et al. (2014) ended up
285 playing leading roles in our high latitude forcing cases (Fig. 3). One likely culprit is the positive
286 ice–albedo feedback, which counteracts the negative SST–OLR feedback. It is unclear whether
287 the resilient net TOA response across our simulations is a coincidence, or an intrinsic feature of
288 the Earth’s climate system in the limit of fully interactive radiative/convective/SST feedbacks; this
289 could be worth more study. Regardless, our findings about partitioning do not depend on the net
290 TOA response magnitude having turned out this way (Fig. 9 and Fig. S3).

291 Meanwhile, the damped SST response in our simulations highlights the importance of the ocean
292 circulation’s role in the global energy budget. Ocean dynamics limit excessive local storage of
293 heat near the surface by redistributing it vertically and horizontally. We have focused on the
294 striking role of overturning circulations in this regard, but the role of gyre circulations would also
295 be an interesting direction for future work to further understand the ocean’s role in ITCZ shift
296 buffering. While the subtropical gyre circulations do not participate much in the direct (advective)
297 heat exchange across the equator, they can non-locally affect both the atmospheric and oceanic
298 column energy budgets via SST-dependent feedbacks, such as through SST–low cloud feedbacks

299 modulated by gyre currents that carry anomalously heated surface water away from radiative action
300 centers (Mechoso et al. 2016). Indeed, such linkages occur in our experiments (Fig. 11).

301 It is worth commenting on the utility of using a theoretical framework pinned on equatorial
302 atmospheric net energy input (NEI_{eq}) to interpret our simulations. NEI_{eq} has been argued to deter-
303 mine the sensitivity of the latitude of the zonal-mean ITCZ (ϕ_{ITCZ}) to a given magnitude of AHT_{eq}
304 perturbation, i.e. $\phi_{ITCZ} \sim \frac{AHT_{eq}}{NEI_{eq}}$ (Bischoff and Schneider 2014). NEI_{eq} is also known to correlate
305 with the hemispherically symmetric component of tropical precipitation biases including the dou-
306 ble ITCZ bias (Adam et al. 2016, 2017). We hypothesize that variations in the NEI_{eq} response to
307 solar forcing do not play a leading role in our experiments based on the quasi-linear relationship
308 between interannual PAI vs. global OHT_{eq} responses (Fig. 9d, f). Consistent with this view, the
309 fractional response of NEI_{eq} is much smaller than that of AHT_{eq} (Fig. 12). However, we acknowl-
310 edge that effects of NEI_{eq} are important and may be responsible for the deviation from the linear
311 regression line, since changes in NEI_{eq} can cause ITCZ shifts independent of changes in AHT_{eq} .

312 An obvious limitation of this study is the use of a single climate model, which raises the ques-
313 tion of whether similar responses should be expected in other climate models. On the one hand,
314 a satisfying answer on inter-model spread will only be gleaned from focused intercomparison,
315 which will be forthcoming via a new Extratropical-Tropical Interaction Model Intercomparison
316 Project. This community activity will include analysis of atmosphere-ocean partitioning of the en-
317 ergy transport response to extratropical TOA perturbation [Sarah Kang, personal communication,
318 2017]. On the other hand, it is also already logical to expect some degree of similar responses to
319 occur across independent models. Despite the fact that the temporal mean structure and variabil-
320 ity of the AMOC varies widely among Coupled Model Intercomparison Project version 3 and 5
321 (CMIP3 and 5) models (Medhaug and Furevik 2011; Zhang and Wang 2013; Muir and Fedorov
322 2015), the AMOC's response to differing forms of radiative forcing tends to share a common sign.

323 Across CMIP5 models, anthropogenic CO₂ forcing tends to weaken the AMOC (Gregory et al.
324 2005; Cheng et al. 2013), and volcanic aerosol forcing strengthens it (Ding et al. 2014) while also
325 shifting the ITCZ towards the hemisphere opposite to eruption (Iles and Hegerl 2014). Anthro-
326 pogenic aerosol forcing has also been shown to strengthen the AMOC across a set of independent
327 studies that used different coupled GCMs (e.g. GFDL CM2.1 (Delworth and Dixon 2006), CSIRO
328 Mk2.1 (Cowan and Cai 2013), and HadGEM2-ES (Menary et al. 2013)). Especially considering
329 that our TOA solar perturbation shares some similarities to a geographically confined aerosol ra-
330 diative forcing, these are all reasons to expect the sensitivity we have shown in CESM should be
331 detectable in other CMIP5-class climate models.

332 Another limitation of this work is that it does not attempt to fully attribute the mechanistic path-
333 way connecting regional TOA solar forcing to varying degrees of AMOC response. While beyond
334 scope, we view it as an interesting topic worthy of future work, via process analysis focused on
335 subducting regions. As expected from cooling of the North Atlantic, positive regional anomalies of
336 surface ocean density over the Labrador Sea deep water formation region lead AMOC responses
337 in all our experiments (Fig. 13). But the origin of these density perturbations in the Labrador
338 Sea is not immediately obvious, especially in the case of low-latitude forcing experiments where
339 solar perturbations are applied away from the deep water formation regions. Relevant processes
340 are likely to include advection of buoyancy anomalies through subtropical and subpolar gyres
341 and regional meteorological changes via tropical-extratropical teleconnection. Future work fo-
342 cusing on these mechanistic process chains might help contribute to further understanding of the
343 AMOC–ITCZ nexus. Another caveat of our experimental design is that the TROP forcing some-
344 what awkwardly attempts to force a sharp thermal gradient near the equator. On the one hand,
345 the actual near-equatorial SST gradient response of this subexperiment is not an outlier relative to
346 our other simulations, which suggests sharp thermal gradients are efficiently buffered by dynamics

347 that must resist them near the equator (Fig. 14). Nonetheless, future iterations of this experiment
348 design would benefit from avoiding this technical issue.

349 A final limitation is our use of idealized, geographically localized forcing bands to probe the
350 coupled system's dynamics. It is natural to wonder to what degree this informs understanding of
351 the system's sensitivity to more realistic sources of interhemispherically asymmetric solar forcing
352 like volcanoes or geo-engineering. In this context we suggest it may be possible to think of our
353 experiments as akin to Green's functions, or kernels, in that they have some demonstrable additive
354 utility. That is, the results of the WHOLE experiment, in which we perturb each entire hemisphere
355 at one quarter the power magnitude of the four regional sub-experiments, reproduces to a remark-
356 able degree the linear average of those four experiments' independent responses (e.g. Figs. 6, 7,
357 and 3). This implies some generality beyond our idealized setup that could be practically rele-
358 vant to many realistic forcing contexts; the idea of kernels summarizing these dynamics is worth
359 exploring more.

360 Notwithstanding such limitations, one implication of our results relates to improving tropical
361 rainfall biases in coupled GCMs. Our results, along with recent coupled GCM studies (Kay et al.
362 2016; Hawcroft et al. 2016, 2018), seem to challenge the notion that *high-latitude* cloud radiative
363 biases play a controlling role on biases of tropical precipitation, a view that has been supported
364 by correlations across CMIP5 models (Hwang and Frierson 2013). Our experiments imply the op-
365 posite, given that the AMOC response can provide an efficient buffer to ITCZ shifts when hemi-
366 spherically asymmetric radiative forcing biases are concentrated at high latitudes. The reduction of
367 this oceanic buffering pathway when the same interhemispheric forcing is focused at low latitudes
368 implies that even a small bias in cloud radiative forcing near the tropics might induce a strong at-
369 mospheric (ITCZ shift) response. This appears consistent with the findings of Xiang et al. (2017)
370 who argued that across CMIP5 models, the degree of the double ITCZ bias of coupled models is

371 better predicted by the hemispheric asymmetry of their net TOA shortwave fluxes near the tropics
372 in atmosphere-only simulations, than by those in the extratropics. It also evokes the findings of
373 Mechoso et al. (2016) who showed stratocumulus cloud biases in the subtropics can overwhelm
374 modifications to southern ocean radiative forcing. Together, these results support renewed focus
375 on improving *low-latitude* radiation biases towards improving tropical precipitation.

376 **5. Conclusion**

377 We have shown results from a comprehensive global climate model that reveals the AMOC can
378 be especially important in setting the degree to which ocean dynamics act to damp radiatively
379 forced migrations of the zonal-mean ITCZ. This effect becomes strong when an interhemispheri-
380 cally asymmetric forcing is focused at high latitudes, highlighting the importance of the meridional
381 distribution of shortwave radiative forcing in such dynamics. The main implication is that ongoing
382 attempts to develop ITCZ migration theory that includes the role of buffering by ocean dynamics
383 may ultimately depend on a satisfying theory for the AMOC's response to radiative forcing, and
384 its links to the ITCZ. Another practical implication for near-term GCM development is that fixing
385 low-latitude TOA radiative biases in climate models might be a more practical strategy towards
386 improving tropical rainfall biases than fixing high-latitude biases.

387 *Acknowledgments.* We would like to acknowledge François Primeau for helpful discussions.
388 This work was funded by National Science Foundation AGS-1419518. Model simulations were
389 done in Yellowstone (ark:/85065/d7wd3xhc) provided by NCAR's CISL, sponsored by the Na-
390 tional Science Foundation.

391 BibTeX. It uses references.bib and the ametsoc2014.bst file for the style.

392 **References**

- 393 AA, M., and D. W. Frierson, 2017: The role of ocean fluxes and radiative forcings in de-
394 termining tropical rainfall shifts in RCP8.5 simulations. *Geophysical Research Letters*, doi:
395 10.1002/2017GL074473.
- 396 Adam, O., T. Schneider, and F. Brient, 2017: Regional and seasonal variations of the double-ITCZ
397 bias in CMIP5 models. *Clim. Dyn.*, 1–17, doi:10.1007/s00382-017-3909-1.
- 398 Adam, O., T. Schneider, F. Brient, and T. Bischoff, 2016: Relation of the doubleITCZ bias to the
399 atmospheric energy budget in climate models. *Geophys Res Lett*, doi:10.1002/2016GL069465.
- 400 Allen, R. J., 2015: A 21st century northward tropical precipitation shift caused by future an-
401 thropogenic aerosol reductions. *Journal of Geophysical Research: Atmospheres*, doi:10.1002/
402 2015JD023623.
- 403 Bischoff, T., and T. Schneider, 2014: Energetic constraints on the position of the intertropical
404 convergence zone. *Journal of Climate*, **27** (13), 4937–4951, doi:10.1175/JCLI-D-13-00650.1.
- 405 Broccoli, A., K. Dahl, and R. Stouffer, 2006: Response of the ITCZ to northern hemisphere
406 cooling. *Geophys. Res. Lett.*, **33**, L01 702, doi:10.1029/2005GL024546.
- 407 Buckley, M., and J. Marshall, 2016: Observations, inferences, and mechanisms of the at-
408 lantic meridional overturning circulation: A review. *Rev. Geophys.*, **54**, 5–63, doi:10.1002/
409 2015RG000493.
- 410 Ceppi, P., Y. Hwang, X. Liu, D. M. Frierson, and D. L. Hartmann, 2013: The relationship between
411 the ITCZ and the southern hemispheric eddydriven jet. *J Geophys Res Atmospheres*, **118** (11),
412 5136–5146, doi:10.1002/jgrd.50461.

- 413 Chang, P., and Coauthors, 2008: Oceanic link between abrupt changes in the north atlantic ocean
414 and the african monsoon. *Nature Geoscience*, **1** (7), 444–448, doi:10.1038/ngeo218.
- 415 Cheng, W., J. C. H. Chiang, and D. Zhang, 2013: Atlantic meridional overturning circulation
416 (AMOC) in CMIP5 models: RCP and historical simulations. *Journal of Climate*, **26** (18), 7187–
417 7197, doi:10.1175/JCLI-D-12-00496.1.
- 418 Chiang, J. C., and C. M. Bitz, 2005: Influence of high latitude ice cover on the marine intertropical
419 convergence zone. *Clim Dynam*, **25** (5), 477–496, doi:10.1007/s00382-005-0040-5.
- 420 Cowan, T., and W. Cai, 2013: The response of the largescale ocean circulation to 20th century
421 asian and nonAsian aerosols. *Geophys Res Lett*, **40** (11), 2761–2767, doi:10.1002/grl.50587.
- 422 Cvijanovic, I., P. L. Langen, E. Kaas, and P. D. Ditlevsen, 2013: Southward intertropical con-
423 vergence zone shifts and implications for an atmospheric bipolar seesaw. *J Climate*, **26** (12),
424 4121–4137, doi:10.1175/JCLI-D-12-00279.1.
- 425 Delworth, T. L., and K. W. Dixon, 2006: Have anthropogenic aerosols delayed a greenhouse gas-
426 induced weakening of the north atlantic thermohaline circulation? *Geophys. Res. Lett.*, **33** (2),
427 doi:10.1029/2005GL024980.
- 428 Ding, Y., J. A. Carton, G. A. Chepurin, G. Stenchikov, A. Robock, L. T. Sentman, and J. P.
429 Krasting, 2014: Ocean response to volcanic eruptions in coupled model intercomparison project
430 5 simulations. *J. Geophys. Res. Ocean*, **119** (9), 5622–5637, doi:10.1002/2013JC009780.
- 431 Donohoe, A., J. Marshall, and D. Ferreira, 2013: The relationship between ITCZ location and
432 cross-equatorial atmospheric heat transport: From the seasonal cycle to the last glacial maxi-
433 mum. *Journal of Climate*.

- 434 Drijfhout, S. S., 2010: The atmospheric response to a thermohaline circulation collapse: Scaling
435 relations for the hadley circulation and the response in a coupled climate model. *J Climate*,
436 **23 (3)**, 757–774, doi:10.1175/2009JCLI3159.1.
- 437 Dunstone, N., D. Smith, B. Booth, L. Hermanson, and R. Eade, 2013: Anthropogenic aerosol
438 forcing of atlantic tropical storms. *Nat Geosci*, **6 (7)**, 534–539, doi:10.1038/ngeo1854.
- 439 Frierson, D. M. W., and Coauthors, 2013: Contribution of ocean overturning circulation to tropical
440 rainfall peak in the northern hemisphere. *Nat. Geosci*, **6**, doi:10.1038/ngeo1987.
- 441 Fukar, N. S., S. Xie, R. Farneti, E. A. Maroon, and D. M. Frierson, 2013: Influence of the extrat-
442 ropical ocean circulation on the intertropical convergence zone in an idealized coupled general
443 circulation model. *J. Climate*, **26 (13)**, 4612–4629, doi:10.1175/JCLI-D-12-00294.1.
- 444 Green, B., and J. Marshall, 2017: Coupling of trade winds with ocean circulation damps ITCZ
445 shifts. *J Climate*, doi:10.1175/JCLI-D-16-0818.1.
- 446 Gregory, J., and Coauthors, 2005: A model intercomparison of changes in the atlantic thermoha-
447 line circulation in response to increasing atmospheric CO₂ concentration. *Geophys. Res. Lett.*,
448 **32 (12)**, L12 703, doi:10.1029/2005GL023209.
- 449 Hawcroft, M., J. Haywood, M. Collins, and A. Jones, 2016: Southern ocean albedo, inter-
450 hemispheric energy transports and the double ITCZ: global impacts of biases in a coupled
451 model. *Climate Dynamics*, doi:10.1007/s00382-016-3205-5.
- 452 Hawcroft, M., J. M. Haywood, M. Collins, and A. Jones, 2018: The contrasting climate re-
453 sponse to tropical and extratropical energy perturbations. *Climate Dynamics*, doi:10.1007/
454 s00382-018-4076-8.

455 Haywood, J. M., and Coauthors, 2016: The impact of equilibrating hemispheric albedos on trop-
456 ical performance in the HadGEM2 ES coupled climate model. *Geophys. Res. Lett.*, **43** (1),
457 395–403, doi:10.1002/2015GL066903.

458 Held, I., 2001: The partitioning of the poleward energy transport between the tropical ocean
459 and atmosphere. *Journal of the atmospheric sciences*, doi:10.1175/1520-0469(2001)058<0943:
460 TPOTPE>2.0.CO;2.

461 Hurrell, J. W., and Coauthors, 2013: The community earth system model: A framework for col-
462 laborative research. *Bulletin of the American Meteorological Society*, **94** (9), 1339–1360, doi:
463 10.1175/BAMS-D-12-00121.1.

464 Hwang, Y., and D. Frierson, 2013: Link between the double-Intertropical convergence zone prob-
465 lem and cloud biases over the southern ocean. *Proceedings of the National* , **10** (13), 4935–4940,
466 doi:10.1073/pnas.1213302110.

467 Iles, C., and G. Hegerl, 2014: The global precipitation response to volcanic eruptions in the CMIP5
468 models. *Environmental Research Letters*, **9**, 104 012 (10pp).

469 JP, M., and P. Lu, 1994: Interaction between the subtropical and equatorial ocean circula-
470 tions: The subtropical cell. *Journal of Physical Oceanography*, **24**, 466–497, doi:10.1175/
471 1520-0485(1994)024<0466\;IBTSAE>2.0.CO.

472 Kang, S., I. Held, D. Frierson, and M. Zhao, 2008: The response of the ITCZ to extratropical
473 thermal forcing: Idealized slab-ocean experiments with a GCM. *Journal of Climate*.

474 Kang, S. M., Y. Shin, and S. Xie, 2018: Extratropical forcing and tropical rainfall distribution:
475 energetics framework and ocean ekman advection. *npj Climate and Atmospheric Science*, **1** (1),
476 doi:10.1038/s41612-017-0004-6.

477 Kay, J. E., C. Wall, V. Yettella, B. Medeiros, C. Hannay, P. Caldwell, and C. Bitz, 2016: Global
478 climate impacts of fixing the southern ocean shortwave radiation bias in the community earth
479 system model (CESM). *Journal of Climate*, **29** (12), 4617–4636, doi:10.1175/JCLI-D-15-0358.
480 1.

481 Liu, Z., and S. G. H. Philander, 1995: How different wind stress patterns affect the tropical-
482 subtropical circulations of the upper ocean. *Journal of physical oceanography*, doi:10.1175/
483 1520-0485(1995)025<0449:HDWSPA>2.0.CO;2.

484 Manabe, S., and R. Stouffer, 1995: Simulation of abrupt climate change induced by freshwater
485 input to the north atlantic ocean. *Nature*, **378**.

486 Marshall, J., A. Donohoe, D. Ferreira, and M. D, 2014: The ocean’s role in setting the mean
487 position of the Inter-Tropical convergence zone. *Climate Dynamics*, **42**, 1967–1979, doi:10.
488 1007/s00382-013-1767-z.

489 Mechoso, C., and Coauthors, 2016: Can reducing the incoming energy flux over the southern
490 ocean in a CGCM improve its simulation of tropical climate? *Geophys Res Lett*, **43** (20), doi:
491 10.1002/2016GL071150.

492 Medhaug, I., and T. Furevik, 2011: North atlantic 20th century multidecadal variability in coupled
493 climate models: sea surface temperature and ocean overturning circulation. *Ocean Sci.*, **7** (3),
494 389–404, doi:10.5194/os-7-389-2011.

495 Menary, M., and Coauthors, 2013: Mechanisms of aerosolforced AMOC variability in a state of
496 the art climate model. *Journal of*, **118**, 2087–2096, doi:10.1002/jgrc.20178.

497 Merlis, T. M., M. Zhao, and I. M. Held, 2013: The sensitivity of hurricane frequency to ITCZ
498 changes and radiatively forced warming in aquaplanet simulations. *Geophys Res Lett*, **40** (15),
499 4109–4114, doi:10.1002/grl.50680.

500 Miyama, T., M. Julian, T. Jensen, J. Loschnigg, S. Godfrey, and A. Ishida, 2003: Structure and
501 dynamics of the Indian-Ocean cross-equatorial cell. *Deep Sea Res Part Ii Top Stud Oceanogr*,
502 **50** (12-13), 2023–2047, doi:10.1016/S0967-0645(03)00044-4.

503 Muir, L., and A. Fedorov, 2015: How the AMOC affects ocean temperatures on decadal to cen-
504 tennial timescales: the north atlantic versus an interhemispheric seesaw. *Clim Dynam*, **45** (1-2),
505 151–160, doi:10.1007/s00382-014-2443-7.

506 Roberts, W. G., P. Valdes, and J. Singarayer, 2016: Can energy fluxes be used to interpret
507 glacial/interglacial precipitation changes in the tropics? *Geophys. Res. Lett.*, **44**, 63736382,
508 doi:10.1002/2017GL073103.

509 Rotstayn, L., M. Collier, and J. Luo, 2015: Effects of declining aerosols on projections of zonally
510 averaged tropical precipitation. *Environmental Research* , **10**, 044 018, doi:10.1088/1748-9326/
511 10/4/044018.

512 Schneider, T., 2017: Feedback of AtmosphereOcean coupling on shifts of the intertropical conver-
513 gence zone. *Geophysical Research Letters*, doi:10.1002/2017GL075817.

514 Schneider, T., T. Bischoff, and G. Haug, 2014: Migrations and dynamics of the intertropical con-
515 vergence zone. *Nature*, doi:10.1038/nature13636.

516 Seo, J., S. Kang, and D. Frierson, 2014: Sensitivity of intertropical convergence zone move-
517 ment to the latitudinal position of thermal forcing. *J Climate*, **27** (8), 3035–3042, doi:
518 10.1175/JCLI-D-13-00691.1.

519 Seo, J., S. Kang, and T. Merlis, 2017: A model intercomparison of the tropical precipitation
520 response to a CO₂ doubling in aquaplanet simulations. *Geophysical Research Letters*, 993–
521 1000, doi:10.1002/2016GL072347.

522 Tomas, R. A., C. Deser, and L. Sun, 2016: The role of ocean heat transport in the global climate
523 response to projected arctic sea ice loss. *Journal of Climate*, **29 (19)**, 6841–6859, doi:10.1175/
524 JCLI-D-15-0651.1.

525 Vellinga, M., and R. Wood, 2002: Global climatic impacts of a collapse of the atlantic thermoha-
526 line circulation. *Climatic change*, **54**, 251–267.

527 Xiang, B., M. Zhao, I. Held, and J. Golaz, 2017: Predicting the severity of spurious 'double
528 ITCZ' problem in CMIP5 coupled models from AMIP simulations. *Geophysical Research* , doi:
529 10.1002/2016GL071992.

530 Zhang, L., and C. Wang, 2013: Multidecadal north atlantic sea surface temperature and atlantic
531 meridional overturning circulation variability in CMIP5 historical simulations. *J. Geophys. Res.:
532 Oceans*, **118**, 5772–5791, doi:10.1002/jgrc.20390.

533 Zhang, R., and T. Delworth, 2005: Simulated tropical response to a substantial weakening of the
534 atlantic thermohaline circulation. *Journal of Climate*, doi:10.1175/JCLI3460.1.

535 Zhang, R., S. Kang, and I. Held, 2010: Sensitivity of climate change induced by the weakening
536 of the atlantic meridional overturning circulation to cloud feedback. *Journal of Climate*, **23 (2)**,
537 378–389, doi:10.1175/2009JCLI3118.1.

538 **LIST OF FIGURES**

539 **Fig. 1.** Schematics of ITCZ shift damping mechanisms involved with (a, b) the subtropical cell, ver-
540 sus (c, d) the Atlantic meridional overturning cell. Red vertical arrows denote a hemispheri-
541 cally asymmetric top-of-atmosphere net radiative perturbation, and blue lines the associated
542 zonal-mean overturning streamline responses. (Top) The subtropical cell (STC) and Hadley
543 cell (HC) are mechanically coupled via zonal surface wind stress such that the STC and
544 HC overturn in the same direction with similar response partitioning. In this limit a spinup
545 of the STC (b) must associate with a spinup of the HC and enhanced demand from addi-
546 tional interhemispheric forcing. (Bottom) In contrast, the Atlantic Meridional Overturning
547 Circulation (AMOC) is not subject to these constraints. A diverse set of response partition-
548 ings is possible. Even with no change in interhemispheric forcing a strengthening AMOC
549 requires a weakening HC (c, d), or vice-versa, due to atmosphere-ocean competition for a
550 fixed amount of required energy transport. That is, the two cells' responses can be prone to
551 negatively covary. 28

552 **Fig. 2.** (a) Zonal-mean, annual-mean top-of-atmophere insolation perturbation (solid line) and net
553 radiative flux responses (dotted line). (b): Zonal-mean, annual-mean precipitation re-
554 sponses. (c): Annual-mean cross-equatorial heat transport responses of total (grey), at-
555 mospheric (blue), and oceanic (brown)—control results are shown as a baseline. 29

556 **Fig. 3.** The decomposition of the annual-mean cross-equatorial total heat transport (HT_{eq}) re-
557 sponses. The HT_{eq} (black) is decomposed into heat transports due to clear-sky shortwave
558 flux (blue), shortwave cloud radiative effect (CRE) (light blue), clear-sky longwave flux
559 (red), longwave CRE (light red), and oceanic heat content trend. Δ means experiment minus
560 control. All radiative fluxes are at the top of atmosphere. Averaging period is from model
561 year 51 to 200. 30

562 **Fig. 4.** Scatter plot between the annual-mean cross-equatorial atmospheric heat transport (AHT_{eq})
563 response and annual-mean maximum meridional mass streamfunction response at the
564 equator—as a proxy of Hadley circulation strength. Empty dots are 15-year running-
565 averaged time-series for year 51–200 and the filled dots are the mean value of them. The
566 strong relationship implies changes in gross moist stability across the experiments are not
567 significant. 31

568 **Fig. 5.** The decomposition of the annaul-mean cross-equatorial atmospheric heat transport (green)
569 into meridional mean circulation (orange) and eddy (blue) components. The eddy compo-
570 nent include both stationary and transient eddies. 32

571 **Fig. 6.** Annual-mean, cross-equatorial oceanic heat transport (OHT) responses of global (a), At-
572 lantic (b), and Pacific-Indian (c) ocean [unit: PW]. Different colors show different compo-
573 nent of OHT: total (red), dynamic (light blue), thermodynamic (deep blue), and nonlinear
574 (green). Yellow dots are for OHT normalized by basin width [unit: 10^{-7} PW / meter]. 33

575 **Fig. 7.** Annual-mean overturning streamfunction responses for Atlantic (a) and Pacific-Indian basin
576 (b). Right most panels are total response of control simulation [unit: Sv]. Warm (cold) colors
577 are signed as clockwise (counter clockwise) circulations. Note that (a) and (b) have different
578 depths and color bars. 34

579 **Fig. 8.** Time series of responses of AMOC strength(a), Atlantic cross-equatorial oceanic heat trans-
580 port (b), Pacific-Indian asymmetric subtropical cell strength (c), and Pacific-Indian cross-
581 equatorial oceanic heat transport (d). A solid line shows 5-year running mean and shading
582 is \pm one 5-year running standard deviation. AMOC strength is defined as a maximum over-

583 turning streamfunction within 30°N to 50°N latitude and 600m to 1400m depth in Atlantic.
584 Pacific-Indian asymmetric subtropical cell strength is defined as a maximum of asymmet-
585 ric component of overturning streamfunction within 7°N to 15°N latitude and 0m to 250m
586 depth in Pacific-Indian. 35

587 **Fig. 9.** Scatter plots of annual-mean time series between tropical precipitation asymmetry index
588 (PAI) and cross-equatorial oceanic heat transport (OHT) during Year 51 to 200. (top pan-
589 els) long-term component defined as 15-year running average; (bottom panels) short-term
590 component defined as anomalies from the long-term component. (a, d) Global ocean; (b, e)
591 Atlantic ocean; (c, f) Pacific and Indian ocean. Regression lines for all experiments (grey)
592 and for each experiment (color) are shown only for relationship whose r^2 is larger than 0.5.
593 (g) shows correlation coefficients, r , of long-term (solid line) and short-term (dashed line)
594 with different running mean windows. Zero running mean window means original time
595 series. Errors bars are 95% confidence interval. 36

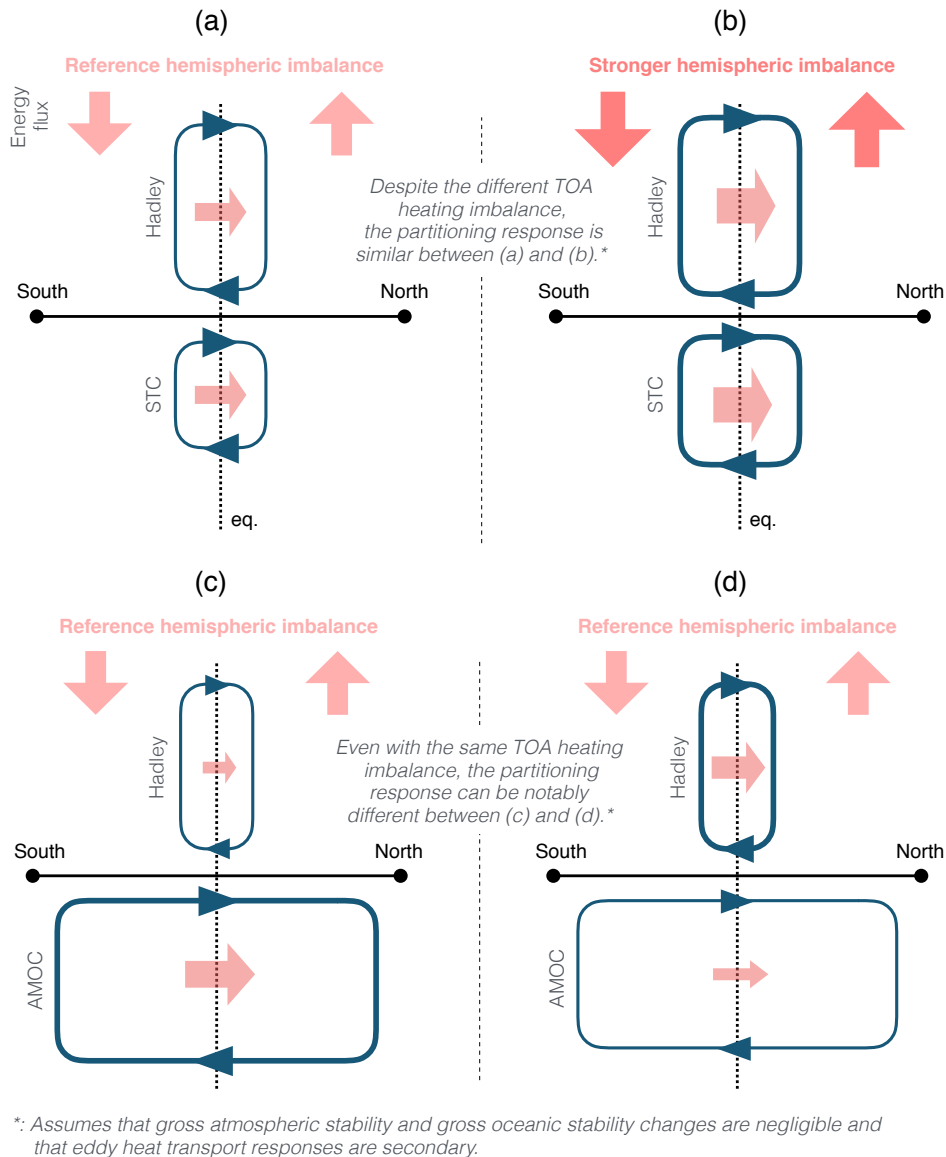
596 **Fig. 10.** Scatter plot between the annual-mean tropical precipitation asymmetry index (PAI) response
597 and the annual-mean cross-equatorial atmospheric heat transport (AHT_{eq}) response. Empty
598 dots are 15-year running-averaged time-series for year 51–200 and the filled dots are the
599 mean value of them. 37

600 **Fig. 11.** Annual mean (a) surface temperature, (b) total cloud fraction, and (c) TOA shortwave cloud
601 radiative effect responses (experiment minus control; except for CTRL) during years 51-200. . . 38

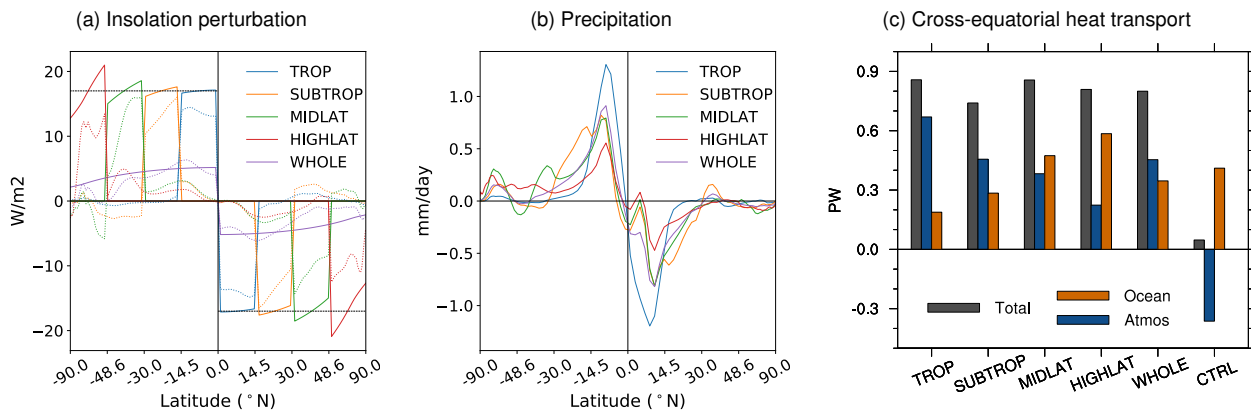
602 **Fig. 12.** Annual-mean (a) NEI_{eq} and (b) AHT_{eq} . Errorbar is showing ± 1 standard deviation of 15-
603 year running-averaged time-series. The averaging period is year 51–200. 39

604 **Fig. 13.** Cross correlation between time series of Labrador Sea upper ocean (0–200m) density and
605 Atlantic meridional overturning circulation (AMOC) strength, smoothed with a 5-year run-
606 ning mean, with negative values indicating Labrador Sea density leading. 40

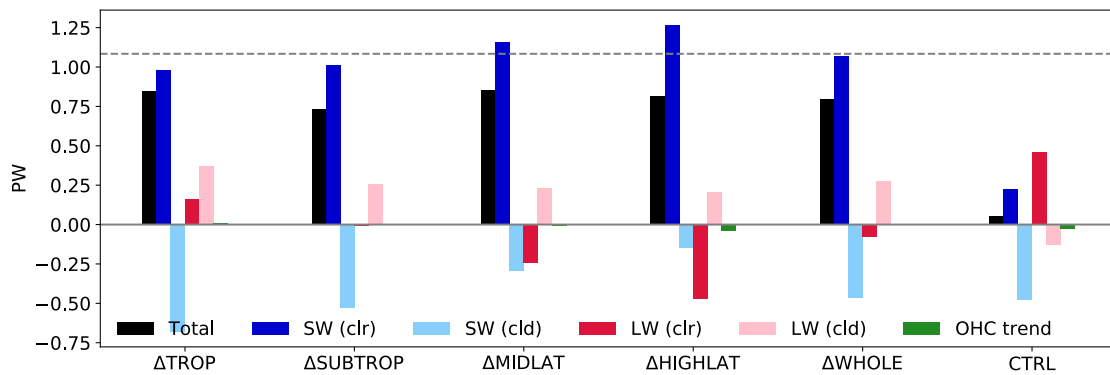
607 **Fig. 14.** The hemispheric asymmetry of annual-mean tropical sea surface temperature (SST) near the
608 equator calculated as the difference of mean SST [$0^\circ, 14.5^\circ$] minus mean SST [$-14.5^\circ, 0^\circ$]
609 during years 51 to 200. 41



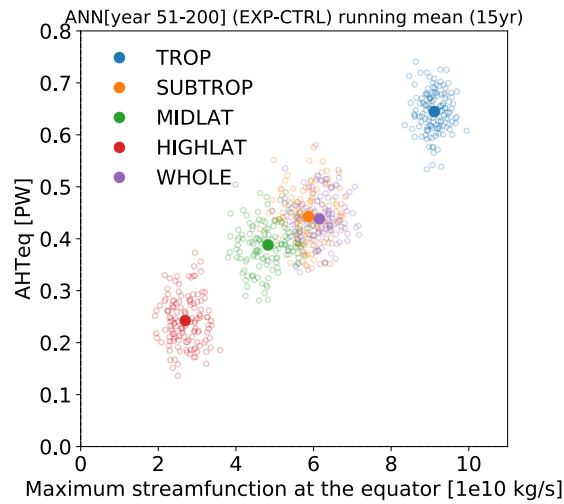
610 FIG. 1. Schematics of ITCZ shift damping mechanisms involved with (a, b) the subtropical cell, versus
 611 (c, d) the Atlantic meridional overturning cell. Red vertical arrows denote a hemispherically asymmetric top-
 612 of-atmosphere net radiative perturbation, and blue lines the associated zonal-mean overturning streamline re-
 613 sponses. (Top) The subtropical cell (STC) and Hadley cell (HC) are mechanically coupled via zonal surface
 614 wind stress such that the STC and HC overturn in the same direction with similar response partitioning. In this
 615 limit a spinup of the STC (b) must associate with a spinup of the HC and enhanced demand from additional
 616 interhemispheric forcing. (Bottom) In contrast, the Atlantic Meridional Overturning Circulation (AMOC) is not
 617 subject to these constraints. A diverse set of response partitionings is possible. Even with no change in interhemi-
 618 spheric forcing a strengthening AMOC requires a weakening HC (c, d), or vice-versa, due to atmosphere-ocean
 619 competition for a fixed amount of required energy transport. That is, the two cells' responses can be prone to
 620 negatively covary.



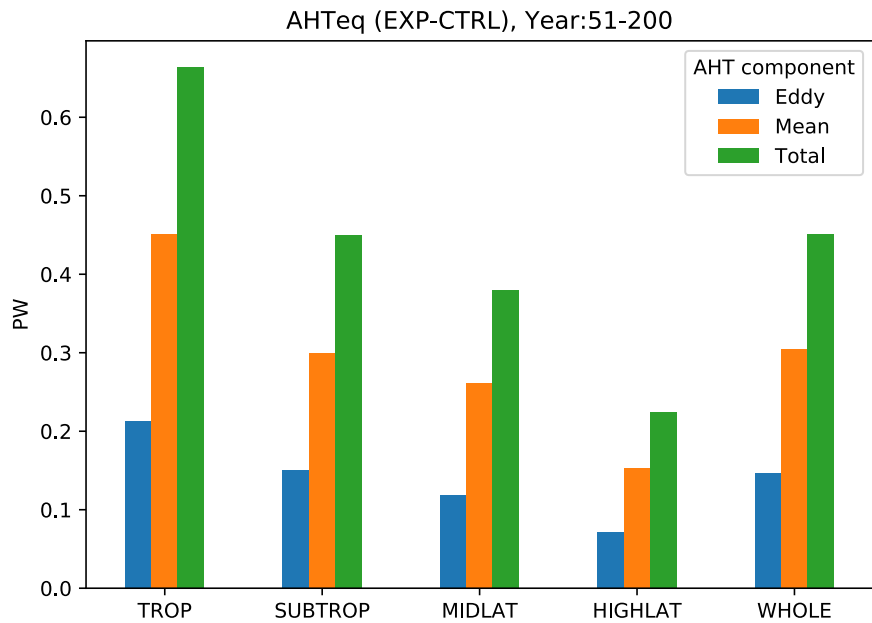
621 FIG. 2. (a) Zonal-mean, annual-mean top-of-atmosphere insolation perturbation (solid line) and net radiative
 622 flux responses (dotted line). (b): Zonal-mean, annual-mean precipitation responses. (c): Annual-mean cross-
 623 equatorial heat transport responses of total (grey), atmospheric (blue), and oceanic (brown)—control results are
 624 shown as a baseline.



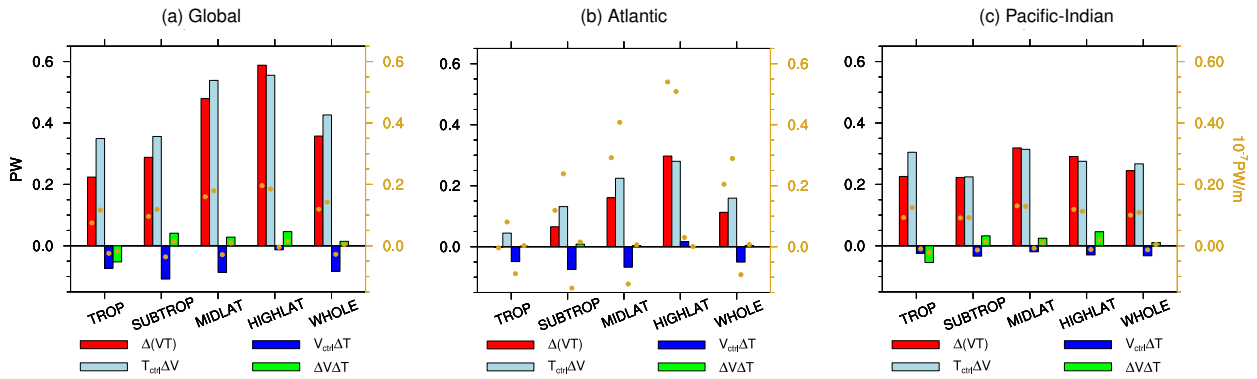
625 FIG. 3. The decomposition of the annual-mean cross-equatorial total heat transport (HT_{eq}) responses. The
 626 HT_{eq} (black) is decomposed into heat transports due to clear-sky shortwave flux (blue), shortwave radiative
 627 effect (CRE) (light blue), clear-sky longwave flux (red), longwave CRE (light red), and oceanic heat content
 628 trend. Δ means experiment minus control. All radiative fluxes are at the top of atmosphere. Averaging period is
 629 from model year 51 to 200.



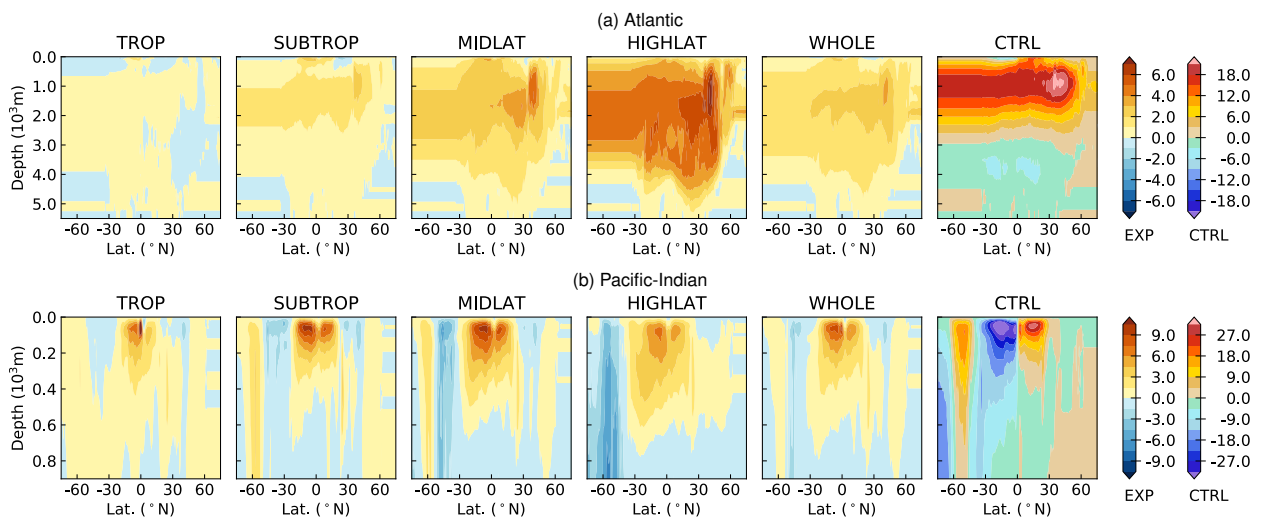
630 FIG. 4. Scatter plot between the annual-mean cross-equatorial atmospheric heat transport (AHT_{eq}) response
 631 and annual-mean maximum meridional mass streamfunction response at the equator—as a proxy of Hadley
 632 circulation strength. Empty dots are 15-year running-averaged time-series for year 51–200 and the filled dots are
 633 the mean value of them. The strong relationship implies changes in gross moist stability across the experiments
 634 are not significant.



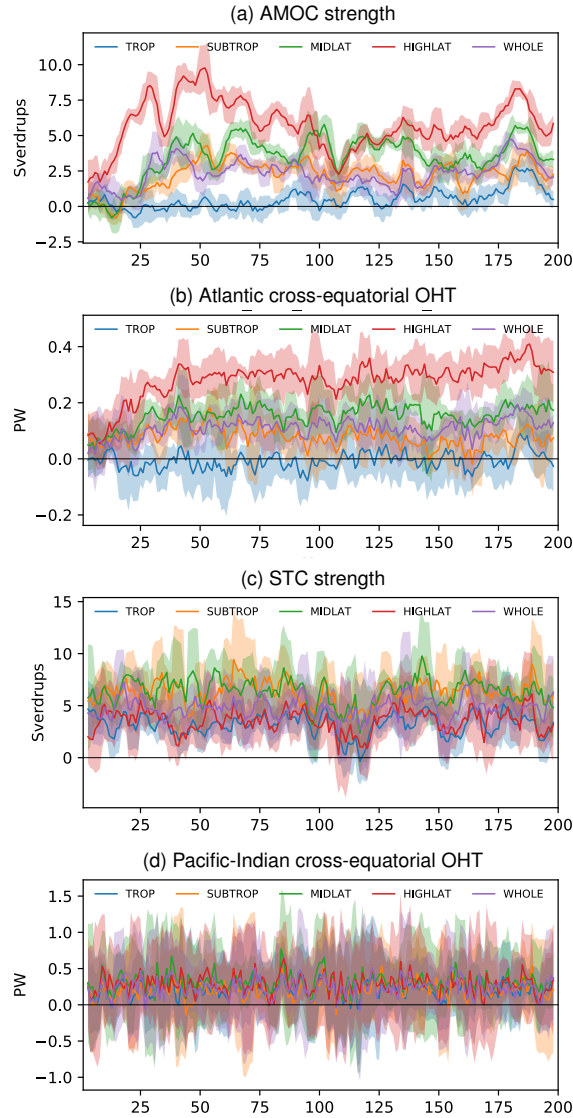
635 FIG. 5. The decomposition of the annular-mean cross-equatorial atmospheric heat transport (green) into merid-
 636 ional mean circulation (orange) and eddy (blue) components. The eddy component include both stationary and
 637 transient eddies.



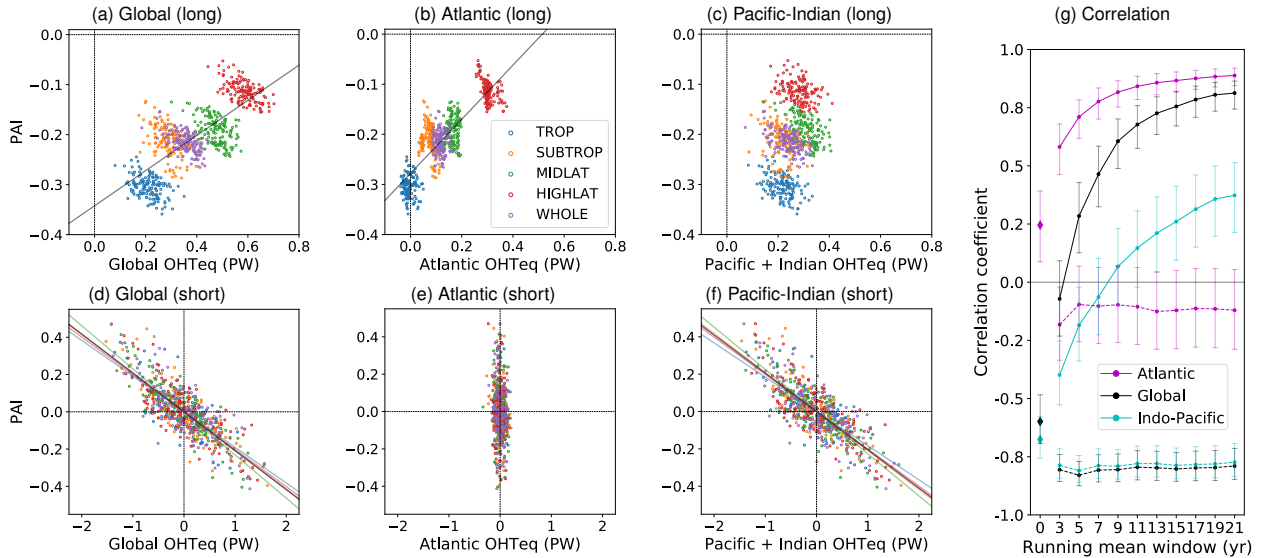
638 FIG. 6. Annual-mean, cross-equatorial oceanic heat transport (OHT) responses of global (a), Atlantic (b), and
 639 Pacific-Indian (c) ocean [unit: PW]. Different colors show different component of OHT: total (red), dynamic
 640 (light blue), thermodynamic (dark blue), and nonlinear (green). Yellow dots are for OHT normalized by basin
 641 width [unit: 10^{-7} PW / meter].



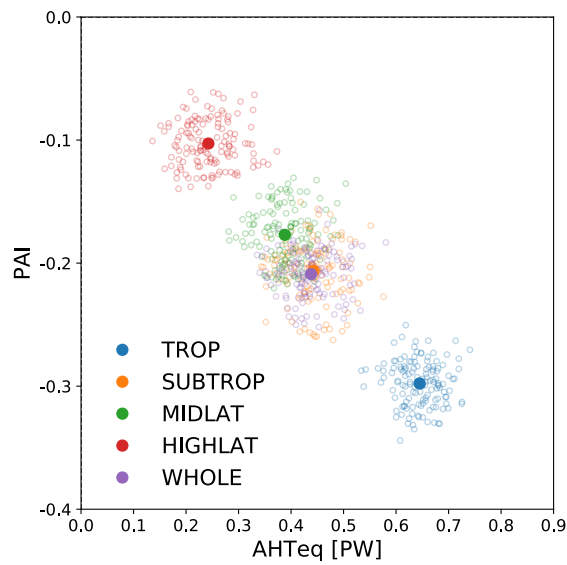
642 FIG. 7. Annual-mean overturning streamfunction responses for Atlantic (a) and Pacific-Indian basin (b). Right
 643 most panels are total response of control simulation [unit: Sv]. Warm (cold) colors are signed as clockwise
 644 (counter clockwise) circulations. Note that (a) and (b) have different depths and color bars.



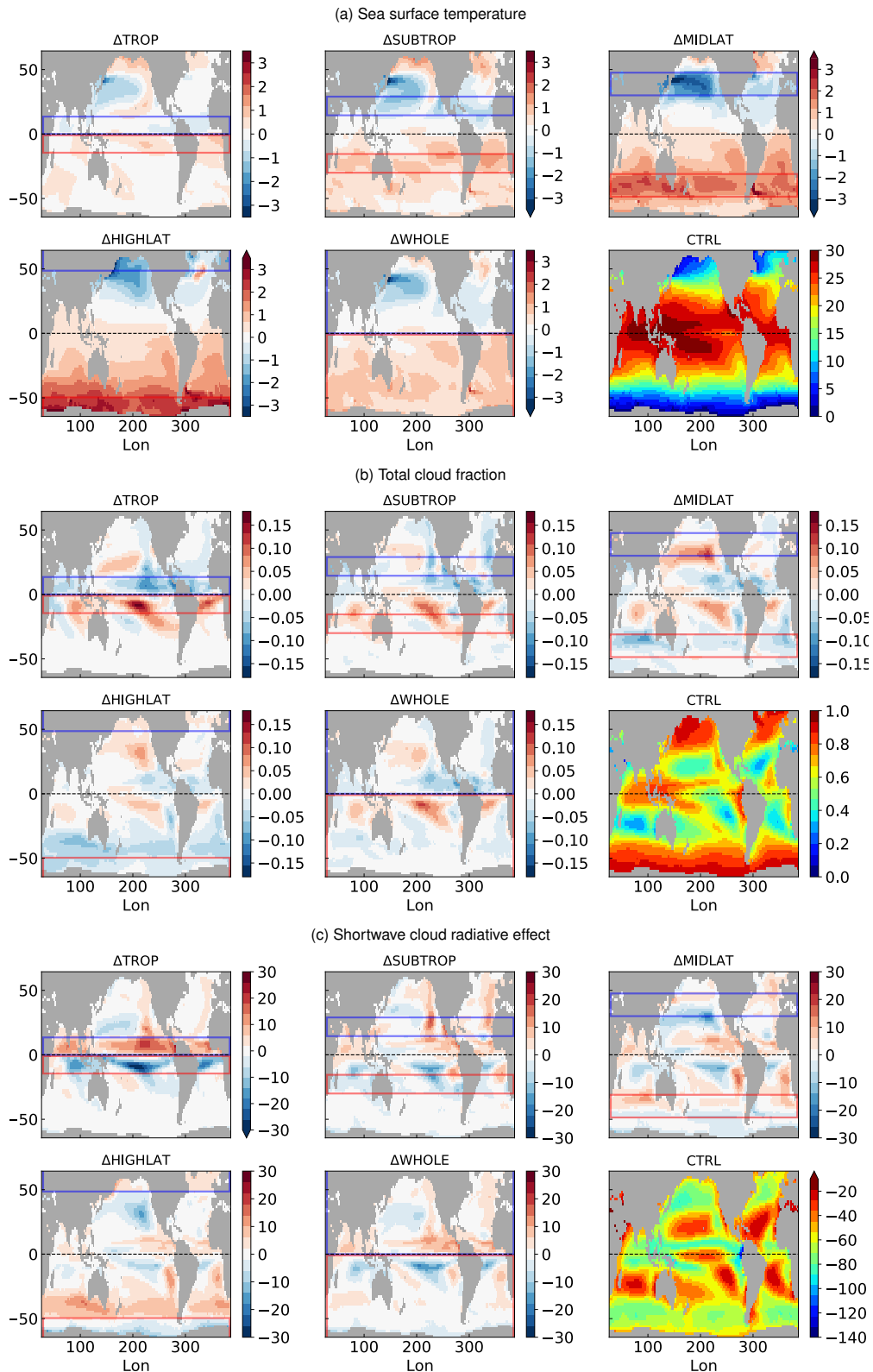
645 FIG. 8. Time series of responses of AMOC strength(a), Atlantic cross-equatorial oceanic heat transport (b),
 646 Pacific-Indian asymmetric subtropical cell strength (c), and Pacific-Indian cross-equatorial oceanic heat transport
 647 (d). A solid line shows 5-year running mean and shading is \pm one 5-year running standard deviation. AMOC
 648 strength is defined as a maximum overturning streamfunction within 30°N to 50°N latitude and 600m to 1400m
 649 depth in Atlantic. Pacific-Indian asymmetric subtropical cell strength is defined as a maximum of asymmetric
 650 component of overturning streamfunction within 7°N to 15°N latitude and 0m to 250m depth in Pacific-Indian.



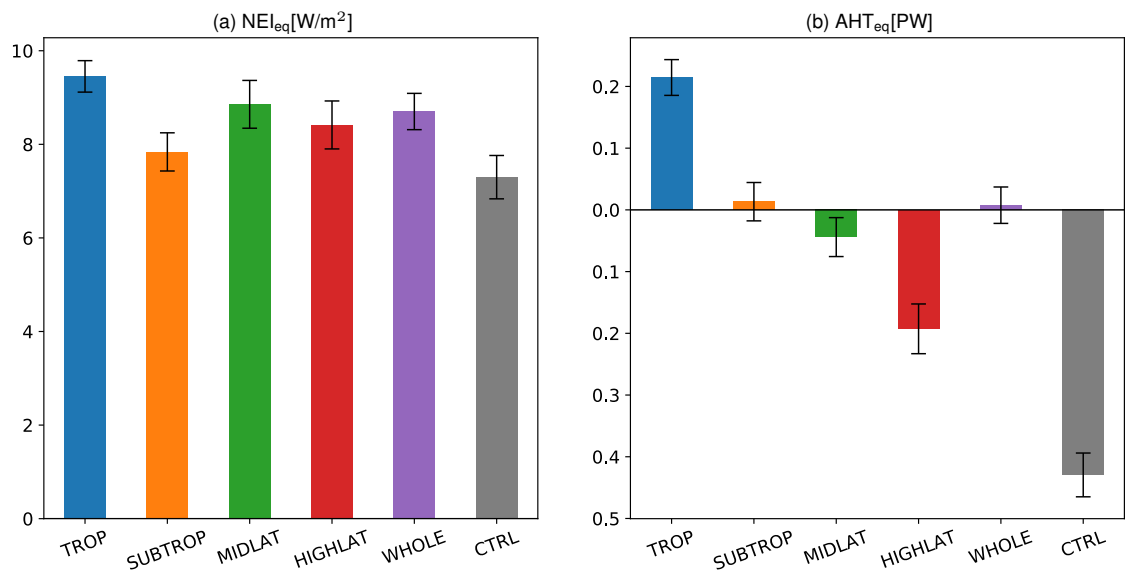
651 FIG. 9. Scatter plots of annual-mean time series between tropical precipitation asymmetry index (PAI) and
 652 cross-equatorial oceanic heat transport (OHT) during Year 51 to 200. (top panels) long-term component defined
 653 as 15-year running average; (bottom panels) short-term component defined as anomalies from the long-term
 654 component. (a, d) Global ocean; (b, e) Atlantic ocean; (c, f) Pacific and Indian ocean. Regression lines for all
 655 experiments (grey) and for each experiment (color) are shown only for relationship whose r^2 is larger than 0.5.
 656 (g) shows correlation coefficients, r , of long-term (solid line) and short-term (dashed line) with different running
 657 mean windows. Zero running mean window means original time series. Errors bars are 95% confidence interval.



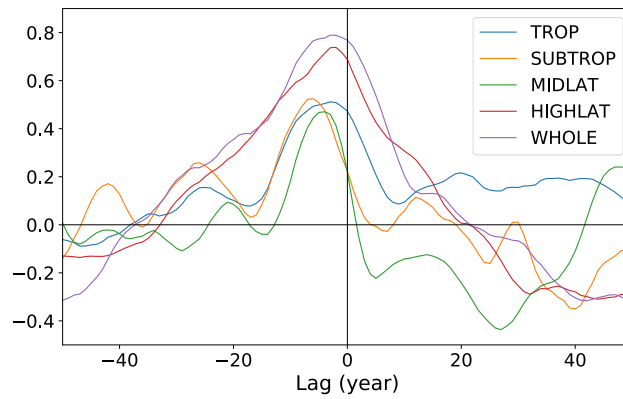
658 FIG. 10. Scatter plot between the annual-mean tropical precipitation asymmetry index (PAI) response and the
 659 annual-mean cross-equatorial atmospheric heat transport (AHT_{eq}) response. Empty dots are 15-year running-
 660 averaged time-series for year 51–200 and the filled dots are the mean value of them.



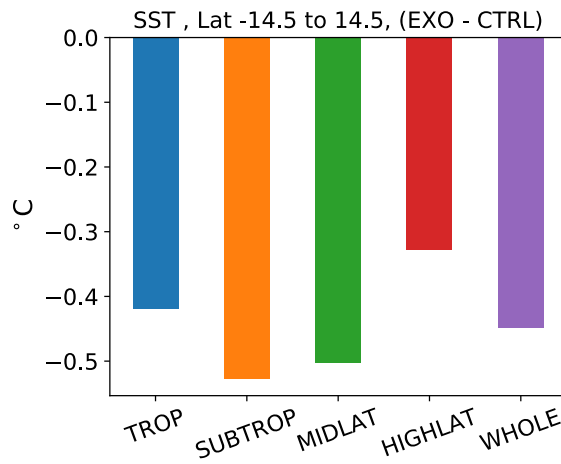
661 FIG. 11. Annual mean (a) surface temperature, (b) total cloud fraction, and (c) TOA shortwave cloud radiative
 662 effect responses (experiment minus control; except for CTRL) during years 51-200.



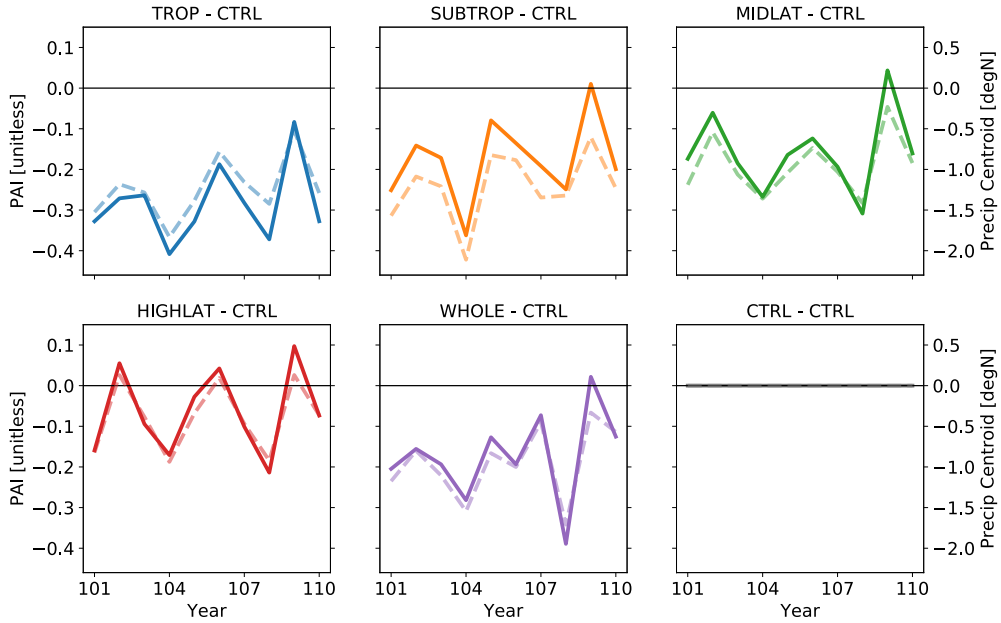
663 FIG. 12. Annual-mean (a) NEI_{eq} and (b) AHT_{eq} . Errorbar is showing ± 1 standard deviation of 15-year
 664 running-averaged time-series. The averaging period is year 51–200.



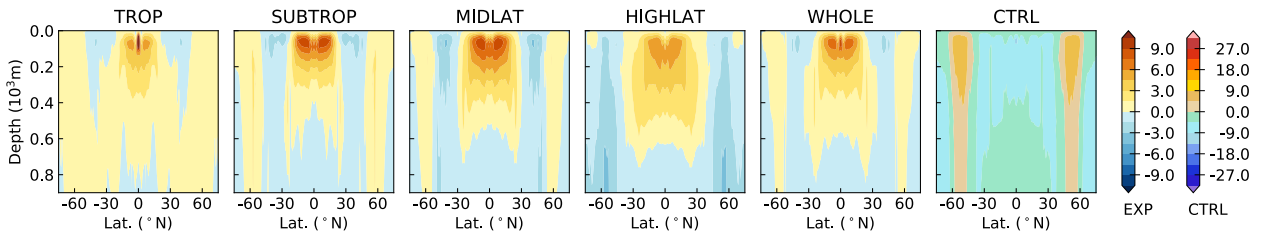
665 FIG. 13. Cross correlation between time series of Labrador Sea upper ocean (0–200m) density and Atlantic
 666 meridional overturning circulation (AMOC) strength, smoothed with a 5-year running mean, with negative val-
 667 ues indicating Labrador Sea density leading.



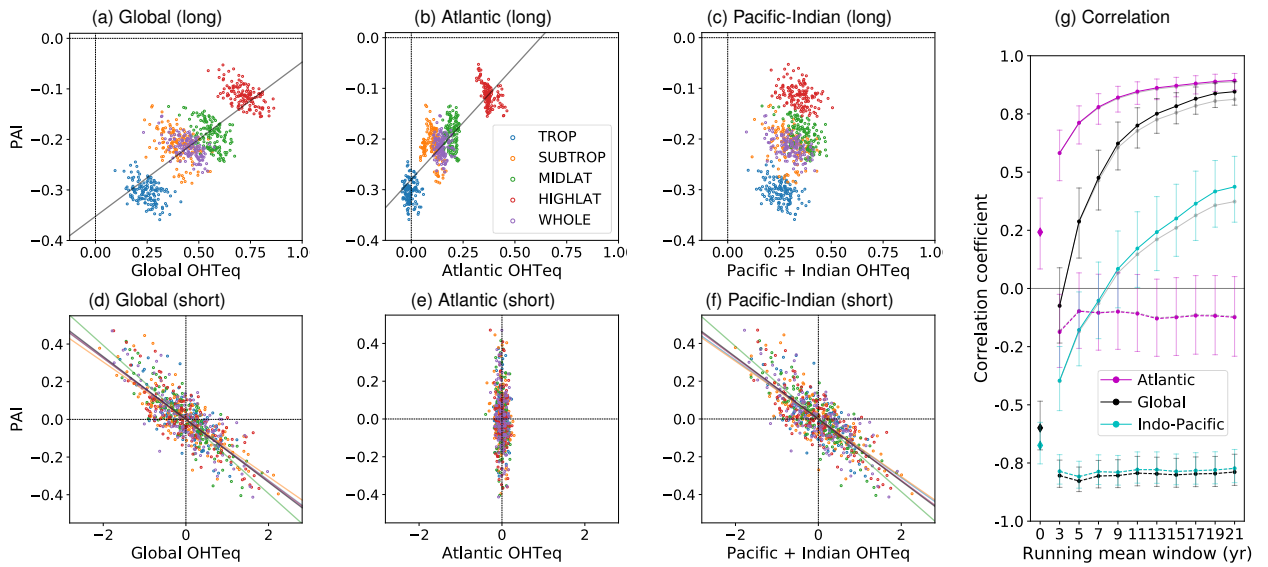
668 FIG. 14. The hemispheric asymmetry of annual-mean tropical sea surface temperature (SST) near the equator
 669 calculated as the difference of mean SST $[0^\circ, 14.5^\circ]$ minus mean SST $[-14.5^\circ, 0^\circ]$ during years 51 to 200.



9 Supplemental Figure S 1. Comparison between (solid) the precipitation asymmetry index and (dashed) pre-
 10 cipitation centroid as alternate measures of the tropical rainfall responses, computed within 20 degrees of the
 11 equator, for an arbitrary time interval of the simulation (years 101-110).



12 Supplemental Figure S 2. Asymmetric component of figure 3b (Pacific-Indian meridional overturning
 13 streamfunction). Following Green and Marshall (2017, J. Climate), Asymmetric component is defined as
 14 $\psi(\phi) = [\psi(\phi) + \psi(-\phi)]/2$, where ψ is overturning streamfunction, and ϕ is latitude.



15 Supplemental Figure S 3. Identical to Fig. 9 except that OHT_{eq} responses are normalized by their respective
 16 total heat transport responses. The grey lines in (g) show the correlation coefficients before normalization, which
 17 are identical to those in Fig. 9g.